APL Photonics

# Selective plane illumination optical endomicroscopy with polymer imaging fibers

Cite as: APL Photonics **8**, 016103 (2023); https://doi.org/10.1063/5.0130486
Submitted: 12 October 2022 • Accepted: 22 November 2022 • Accepted Manuscript Online: 28 November 2022 • Published Online: 13 January 2023

Pablo Roldán-Varona, Calum A. Ross, Luis Rodríguez-Cobo, et al.

# Selective plane illumination optical endomicroscopy with polymer imaging fibers

Cite as: APL Photon. 8, 016103 (2023); doi: 10.1063/5.0130486
Submitted: 12 October 2022 • Accepted: 22 November 2022 •
Published Online: 13 January 2023



Pablo Roldán-Varona,[1,2,3,a] Calum A. Ross,[4] Luis Rodríguez-Cobo,[1] José Miguel López-Higuera,[1,2,3] Erin Gaughan,[5] Kevin Dhaliwal,[5] Michael G. Tanner,[4,5] Robert R. Thomson,[4,5] and Helen E. Parker[4,6]

## AFFILIATIONS

[1] Photonics Engineering Group, Universidad de Cantabria, Santander 39005, Spain
[2] CIBER-bbn, Instituto de Salud Carlos III, Madrid 28029, Spain
[3] Instituto de Investigación Sanitaria Valdecilla (IDIVAL), Santander 39011, Spain
[4] Scottish Universities Physics Alliance (SUPA), Institute of Photonics and Quantum Sciences, Heriot-Watt University, Edinburgh EH14 4AS, United Kingdom
[5] Translational Healthcare Technologies Group, Centre for Inflammation Research, Queen's Medical Research Institute, University of Edinburgh, Edinburgh EH16 4TJ, United Kingdom
[6] *Eunice Kennedy Shriver* National Institute of Child Health and Human Development, National Institutes of Health, Bethesda, MD 20892, USA

**Note:** This paper is part of the APL Photonics Special Topic on Ultrafast Laser Fabrication Enabled Photonics and Devices.
[a] **Authors to whom correspondence should be addressed:** pablo.roldan@unican.es and helen.parker@nih.gov.

## ABSTRACT

Imaging fibers are used to perform real-time fluorescence endomicroscopy, *in vivo*, *in situ*, with the goal of increasing diagnostic information for a plethora of organ systems and diseases. Widefield fiber endomicroscopy systems are simple, cost-effective, and come with fast image acquisition times. However, alternative approaches such as scanning systems produce higher contrast images with intrinsic optical sectioning, improving the visibility of histological features, albeit at the expense of simplicity, cost, and acquisition rate. We developed a selective plane illumination microscopy endoscopic fiber platform, consisting of an ultrafast laser fabricated end-cap, integrated with a polymer coherent fiber bundle, and an epifluorescence microscope. Polymer fibers are known to fluoresce when pumped with blue light, enhancing the background and noise in images. Our end-cap design circumvents this challenge. We demonstrate a reduction of out-of-focus features, along with improved contrast of in-focus features, in images of a tissue phantom. Moreover, we demonstrate the utility of our platform for endomicroscopy using a whole, *ex vivo* human lung model.



## I. INTRODUCTION

Optical fibers are used across a range of clinical applications, due to their flexibility, small cross-section, and ability to reach remote sites in the body. Coherent fiber bundles (CFBs) are a type of optical fiber used for imaging, which consist of an array of many thousands of light-guiding cores. These cores maintain their relative spatial positioning along the length of the bundle, each acting as a pixel in an acquired image. Silica CFBs are used clinically for minimally invasive, fluorescence fiber-bundle endomicroscopy (FBEμ) of various organs of the body,[1,2] providing the opportunity for a better understanding of biological processes. For example, FBEμ has been used within urinary,[3,4] gastrointestinal,[5–10] and respiratory systems,[11–13] for the identification of neoplasia,[3,8,10] dysplasia,[7] cancer,[4,12] infection,[11] or for a more general histological assessment.[5,6,9,13]

Coherent fiber bundles have been used within various endoscopic imaging applications since the late 1950s.[14] However, widespread commercial uptake of CFBs has been hindered by their high cost. Factors determining this cost include the price of the material and the complexity of fabrication. For example, many CFBs are made with highly doped silica cores, in order to maximize

core-cladding refractive index contrast and minimize core crosstalk, which can have a non-negligible effect on imaging performance.[15–17] Such doping is expensive, although impressive advances have been made to realize inexpensive CFBs using low-cost silica preforms intended for telecom fiber.[16,18] Polymer CFBs may be an attractive alternative to silica fibers, as they can enable extremely high core-cladding refractive index contrasts, higher diameter CFBs which maintain relative flexibility, and are fabricated using inherently lower cost materials and facilities. However, it is known that polymer CFBs exhibit substantial fluorescence when pumped with blue light, which can be prohibitive for biological fluorescence imaging, particularly at shorter wavelengths, e.g., green imaging. In order to open up the use of polymer CFBs for low-cost FBEμ, the issue of polymer CFB fluorescence must be overcome.

In fluorescence FBEμ, sample illumination is carried out, conventionally, in either a widefield (WF)[19–21] or scanning[22–25] modality. Widefield systems may be favorable in clinical scenarios, due to their simplicity, low cost, and fast acquisition times. However, image contrast is limited by the presence of out-of-focus fluorescence within highly scattering tissue.[26] Scanning systems allow for optical sectioning, reducing unwanted background, but come with inherently more complex and costly optical arrangements and a decrease in image acquisition rate. On the bench, selective plane illumination microscopy (SPIM) combines speed and simplicity with optical sectioning and high contrast imaging.[27] With this technique, a thin sheet of excitation light is projected across the focal plane, ensuring that the out-of-focus sample is not excited. Accordingly, SPIM requires two orthogonally positioned objectives. To miniaturize and integrate SPIM into the form factor of a fiber-endoscope would, therefore, require a creative solution. To date, efforts toward miniaturized fiber-based SPIM have been directed toward tissue targets in animal models that can be surgically accessed, such as the brain.[28,29] Alternative format, i.e., not fiber-based, miniaturized SPIM implantable devices have been developed for animal studies.[30,31] Although promising, these technologies have cross-sections and optical geometries that are not suitable for minimally invasive delivery through an endoscope in humans.

Ideally, a fluorescence FBEμ system would combine the benefits of several approaches and be cost-effective, be deployable through a conventional endoscope, produce high contrast images, and have a large field of view (FOV), with fast image acquisition. In pursuit of these key features, we have developed a proof-of-concept *SPIM probe,* which consists of a fused silica end-cap and a commercial poly(methyl methacrylate) (PMMA) CFB. The SPIM probe is functional when operated with a bespoke WF epifluorescence microscope. We refer hereafter to the entire SPIM imaging system as the *SPIM probe platform*. While its name highlights its SPIM functionality, it is important to note that our approach also crucially negates the negative effect of CFB fluorescence. Herein, we describe the fabrication of the end-cap by ultrafast laser inscription and selective chemical etching (ULI-CE) and evaluate its performance using a fluorescent tissue phantom. We present images and video data acquired from a whole *ex vivo* human lung model as a proof-of-concept, whereby the SPIM probe was passed to the distal parenchymal region of the human lungs. Thus, we demonstrate that our SPIM probe platform operates within an appropriate regime for the visualization of tissue autofluorescence. This work represents an important step toward the translation of SPIM to *in vivo* scenarios.

## II. RESULTS

### A. Overview of the SPIM probe platform

The SPIM probe platform combines an in-house developed, fused silica end-cap with a PMMA CFB (MCL-1500-1.75, Asahi Kasei Co.) and a custom-built epifluorescence microscope (Fig. 1, see also Methods). A potential clinical deployment strategy of the SPIM probe into the distal lungs via the working channel of a bronchoscope is shown in Fig. 1 (center). Due to its small form factor, the SPIM probe can be delivered directly into the alveolar space [Figs. 1(a) and 1(b)] via a transbronchial pass, where it can visualize endogenous tissue fluorescence. SPIM functionality arises due to the light path through the probe described as follows. The end-cap is affixed to the distal end of the PMMA CFB, shown in Fig. 1(c). The tissue depressed into a shallow front recess is excited by an illumination plane orthogonal to the fiber propagation axis [blue arrows in Fig. 1(c)] via pump light that is coupled at the proximal end to the outer cores only. Fluorescence induced in the illumination plane is collected through a central imaging array of cores of the CFB [green arrows in Fig. 1(c)]. supplementary material video 1 shows an animation of the integration of the fused silica end cap into the CFB (Multimedia view). The SPIM probe platform acquires images in real-time using proximal-end instrumentation consisting of an epifluorescence microscope and computer [Fig. 1(d)]. Figure 1(e) schematically depicts the epifluorescence microscope. For the purposes of this work, we incorporated a second illumination path to straightforwardly convert the platform's operating modality from SPIM to WF, as desired for characterization experiments (see Methods for a complete description).

### B. SPIM probe: Design and fabrication

The end-cap was designed to be secured to the distal tip of the PMMA CFB and to result in SPIM functionality, without adding bulkiness [Fig. 2(a)]. Its key functional feature is an annular, angled mirrored surface that circumscribes the distal end face of the PMMA CFB [Fig. 2(b)] and redirects excitation light into a plane across the FOV. Both the mirrored surface and the peripheral inner surface of the end-cap were given curvatures (radii of curvature 0.45 and 0.15 mm, respectively), to prevent excitation light from diverging excessively outside of the imaging region. The mirrored surface protrudes inwardly to a distance of 70 $\mu$m from the perimeter of the PMMA CFB end face, capping a ring of cores approximately six cores thick. This represents 18% of the total cores in the fiber. Proximally, the epifluorescence system features an axicon lens, in order to couple excitation light only into this ring of cores, delivering excitation to the sample at the distal end. The remaining 82% of the cores is reserved for the collection of fluorescence: This equates to a FOV of ∅ 1.36 mm. The end-cap outer diameter is 1.9 mm [Fig. 2(c)] and can be delivered down the working channel of most commercial bronchoscopes.

The end-cap fabrication process centers around ULI-CE (detailed fully in Methods). Ultrafast laser inscription (ULI)[32] is a powerful technology which enables the production of

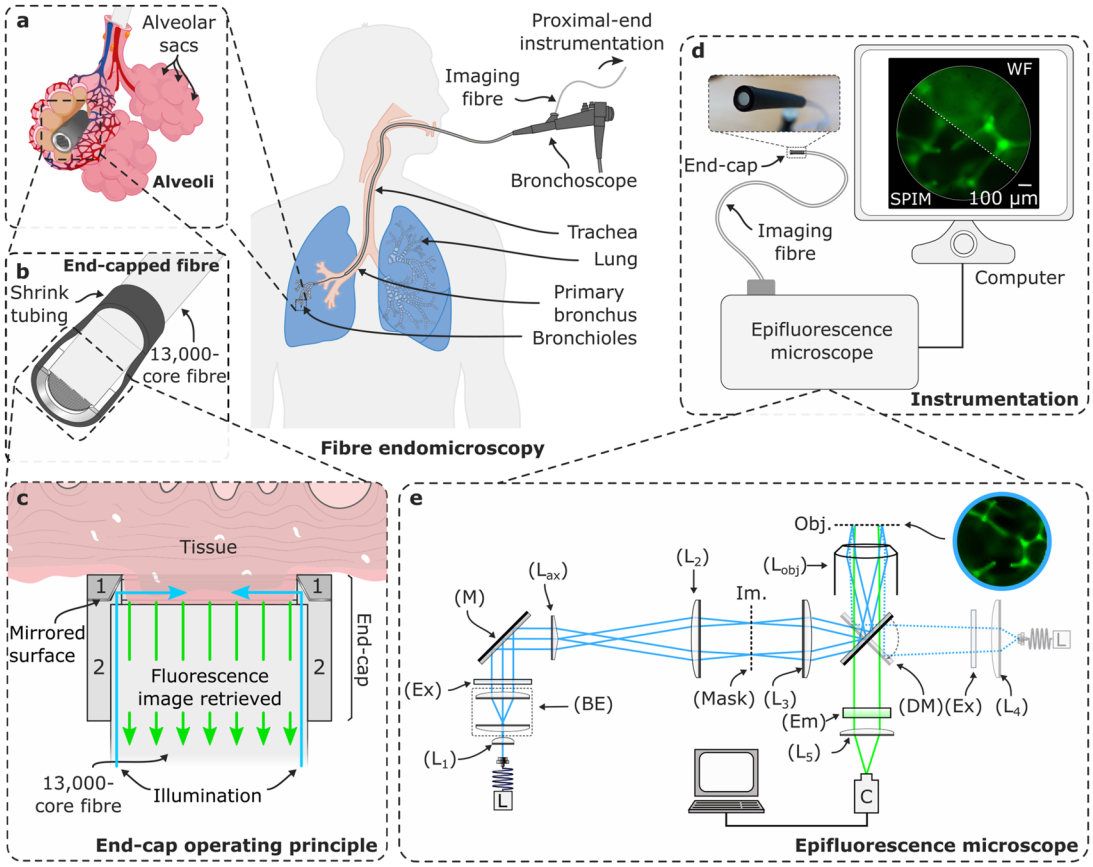


**FIG. 1.** Schematic illustration of the SPIM probe platform for lung imaging. The SPIM probe is intended to be introduced through the working channel of a standard bronchoscope. (a) The diameter of the SPIM probe (1.9 mm) is narrow enough to reach the alveolar space for structural imaging of endogenous fluorescent tissue. (b) The custom-made fused silica end-cap, secured to the distal end of a PMMA imaging fiber. (c) Cross-section of the end-cap when in contact with tissue, showing its operational principle. The end-cap is fabricated in two parts, 1 and 2, between which is a thin mirrored surface. Illumination from a laser, guided by the outer fiber cores, is reflected by the mirrored surface toward the center of the distal tip, generating a light-sheet perpendicular to the direction of observation. Fluorescence from a sample in the front recess of the distal tip is collected through the central column of the cores. (d) The entire SPIM probe platform consists of the SPIM probe (packaged end-cap shown in photo), coupled to an axicon lens-based epifluorescence microscope, and a PC for real-time imaging. (e) Epifluorescence microscope, which enables the SPIM probe [Key: (L) – 485 nm fiber coupled laser, ($L_1$) – lens, (BE) – beam expander, (Ex) – excitation filter, (M) – mirror, ($L_{ax}$) – axicon lens, ($L_2$) – lens, ($L_3$) – lens; (Mask) – silver-coated optical mask, (DM) – dichroic mirror, ($L_{obj}$) – objective lens, (Obj.) – object plane and location of proximal end of SPIM probe, (Em) – emission filter, ($L_5$) – tube lens, (C) – CMOS monochrome camera, and ($L_4$) – tube lens]. Note that the grayed-out illumination path is an integrated WF epifluorescence microscope, which was used for characterization experiments, and is not part of the SPIM probe platform.

micro-optics with remarkable freedom and precision.[33–35] In this technique, tightly focused ultra-short pulses (<350 fs) are used to induce non-linear photoionization in a dielectric substrate.[36–38] The resulting modified substrate volume is highly localized, so that material directly outside of the focal point is largely unaffected. One result of ULI-CE on a substrate is an increased etching rate (up to $\times 10^3$) when compared to pristine material.[39,40] This effect can be harnessed to "write" 3D structures into bulk material, which can then be revealed by wet etching.

In the first part of the fabrication process, the end-cap structure is inscribed into a fused silica substrate as two separate parts [Fig. 2(d)]. Following that, potassium hydroxide (KOH) etching is used to extract the top and bottom parts of the end-cap [Figs. 2(e) and 2(f)]. Silver film deposition is then performed onto the underside of the top part, and the two parts are bonded together before the end-cap is itself bonded to the PMMA CFB [Figs. 2(g) and 2(h), respectively].

### C. SPIM probe characterization: Fluorescence of PMMA CFB, simulation of light field, and core crosstalk measurement

Three aspects of the SPIM probe were characterized. First, we quantified the fluorescence emission of the cores in the PMMA CFB when pumped with blue light. Second, we simulated the distal-end light field of the SPIM probe and compared it with simulations of the CFB fiber when used as a WF imaging fiber. Finally, we investigated the extent of core crosstalk in the PMMA CFB, as a means to compare it with silica CFBs.

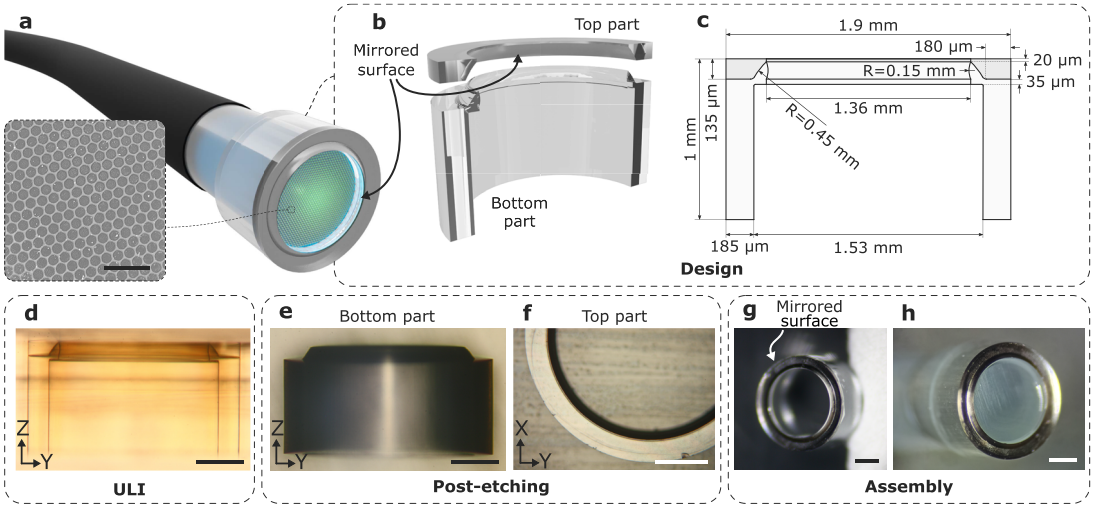


**FIG. 2.** End-cap design and fabrication process. (a) Illustration of the SPIM probe. Inset shows an SEM image of a region of the end face of the fiber. (b) 3D cross-sectional slice of the designed end-cap. The top and bottom parts are shown slightly separated, to indicate the location of a mirrored surface between the two parts. (c) 2D CAD drawing of the end-cap. R refers to radius of curvature. Dimensions are shown to scale. (d) Side view micrograph of the end-cap inscribed in the fused silica substrate. (e) and (f) Micrographs of the bottom and top parts of the end-cap, after KOH etching process. (g) Image of the two parts of the end-cap glued together. A silver thin film is located on the surface between the two parts, as depicted in the illustration in (b). (h) Image of the end-cap bonded to the PMMA CFB. Scale bar in SEM image of (a) is 50 $\mu$m. Scale bars in (d)–(h) are 400 $\mu$m.

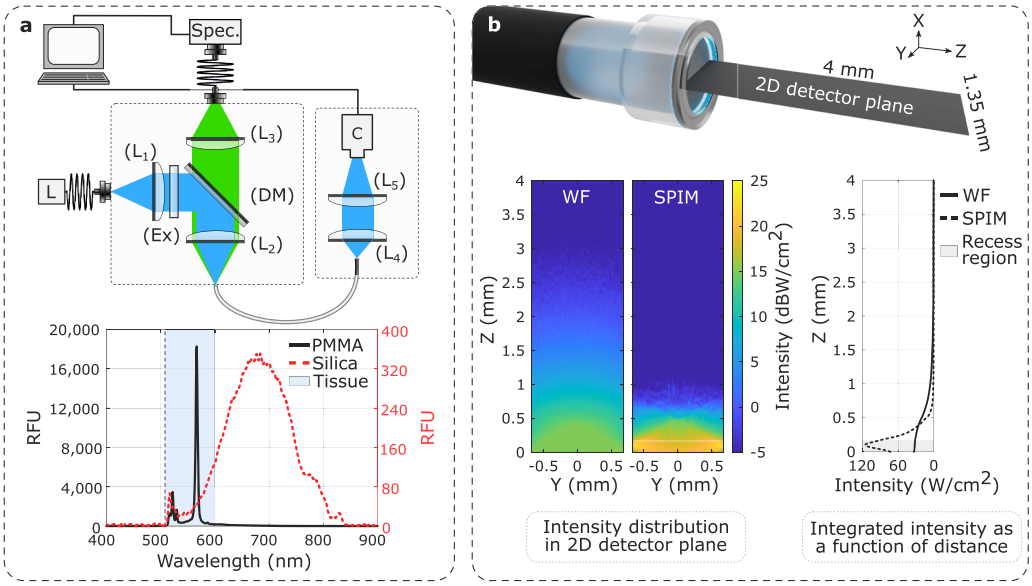


**FIG. 3.** SPIM probe characterization, including measurement of fiber core fluorescence and simulations of light fields in the WF and SPIM cases. (a) Epifluorescence system used to measure the fluorescence emission spectra of the cores of the PMMA CFB and the silica CFB, when pumped with a 485 nm laser [Key: L – 485 nm fiber coupled laser, ($L_{1–5}$) – lenses, (Ex) – excitation filter, (DM) – dichroic mirror, (C) – camera, and (Spec.) – spectrometer]. Plot shows PMMA fiber cores exhibiting a strong green fluorescence (black line) that coincides with the endogenous tissue emission band (blue fill). The silica fiber exhibits a weak, broad fluorescence (red dashed line). Dashed vertical line represents the excitation filter edge. Relative fluorescence unit (RFU) refers to fluorescence counts per meter of fiber. (b) (top) Illustration depicting arrangement of the 4 × 1.35 mm$^2$ ZY rectangular detector in the simulation. (bottom left) 2D simulated excitation light intensity profile in the detector plane, using both WF and SPIM illumination. Absorption/scattering has not been taken into account. Dotted white line at $z$ = 170 $\mu$m on the SPIM profile represents the end of the end-cap. (bottom right) Integrated intensity as a function of distance ($I(z) = (L_y)^{-1} \int_y I(y,z) \cdot dy$, with $L_y$ = 1.35 mm) for WF and SPIM illumination. Front recess region ($z \leq 170$ $\mu$m) is shown as gray fill.

The fluorescence emission from single cores of both the PMMA CFB and a commercial silica CFB (FIGH-30-650S, Fujikura) is shown in Fig. 3(a) (see Methods). When normalized to the length of the fiber, the fluorescence of the PMMA fiber cores was found to be two orders of magnitude greater than that of the silica fiber cores and overlaps with the emission wavelength range of endogenous tissue fluorophores.[41] Thus, using the same cores to provide excitation and to collect fluorescence, as is done in standard WF imaging techniques, would result in a significant fluorescence background and a decreased signal-to-noise ratio. Indeed, this effect can be seen in Figs. 4 and 5, and is discussed later. In contrast, the SPIM probe uses separate sets of cores for excitation and collection, avoiding the negative impact of core fluorescence.

Ray-trace simulations were carried out with the aim of predicting the spatial properties of the excitation plane parallel to the distal end face of the SPIM probe [Fig. 3(b), see also Methods]. We also simulated the case of the PMMA CFB used in a WF modality, i.e., without an end-cap and with proximal-end flood illumination. A simulated detector, perpendicular to the end face of the fiber, shows the intensity distribution in these two scenarios [Fig. 3(b)]. Plots of the intensity distribution in the detector plane and the integrated intensity as a function of distance from the fiber end face allow two key conclusions to be drawn. First, the intensity drop-off as a function of distance is noticeably steeper in SPIM than WF. A 20 dB decay is observed at a distance of ~0.7 mm for SPIM and ~3.3 mm for WF. Second, the power within the front recess of the end-cap ($z \leq 170\ \mu$m) is ~2.97 times higher than that within the equivalent propagation distance in the WF case. According to the simulations, for 1 mW launched into the proximal end of the CFB, 0.232 mW will be confined in the front recess of the SPIM probe compared to 0.078 mW in the equivalent 170 $\mu$m after the fiber at the distal end in the WF case. For an increased distance of 0.5 mm extending from the fiber end face, the power is 0.448 mW in the SPIM case and 0.194 mW in the WF case. In short, almost half of the power delivered in the SPIM probe is confined in the first 0.5 mm after the fiber. Thus, in the SPIM case, distant features in any given FOV receive less light, and more light is contained within the CFB imaging volume. It should be noted that some light exiting the CFB diverges outside of the finite detector plane and is not captured in the simulations.

Silica CFBs are typically designed with a range in core size, as a means to prevent crosstalk, a power-coupling between neighboring cores, which degrades imaging performance. The PMMA CFB features very uniform core size (10.5 $\mu$m, SD = 0.24 $\mu$m) and spacing (1.5 $\mu$m, SD = 0.15 $\mu$m) [extracted from SEM image of Fig. 2(a)]. Core crosstalk of the PMMA CFB at 515 nm was experimentally measured, using a method adapted from Perperidis *et al.*,[15] and subsequently simulated (see supplementary material Note 1). In the experimental method, light was coupled proximally to a single core. At the distal end, light exiting the core, as well as its neighboring cores, was measured. We found that, despite the uniformity of the core pattern in the PMMA CFB and the number of supported modes of the 10.5 $\mu$m cores (~512 at 515 nm) along a 1 m length of fiber, 66.3% ± 2.4% of light coupled into one core of the PMMA CFB remained confined to the core, while the remaining ~33.7% power-coupled to neighboring cores. These values are comparable to the available reported measurements of silica CFBs.[15,16] Thus, it can be expected that image degradation as a result of core crosstalk is no more of a concern using the PMMA CFB than it is using a silica fiber.

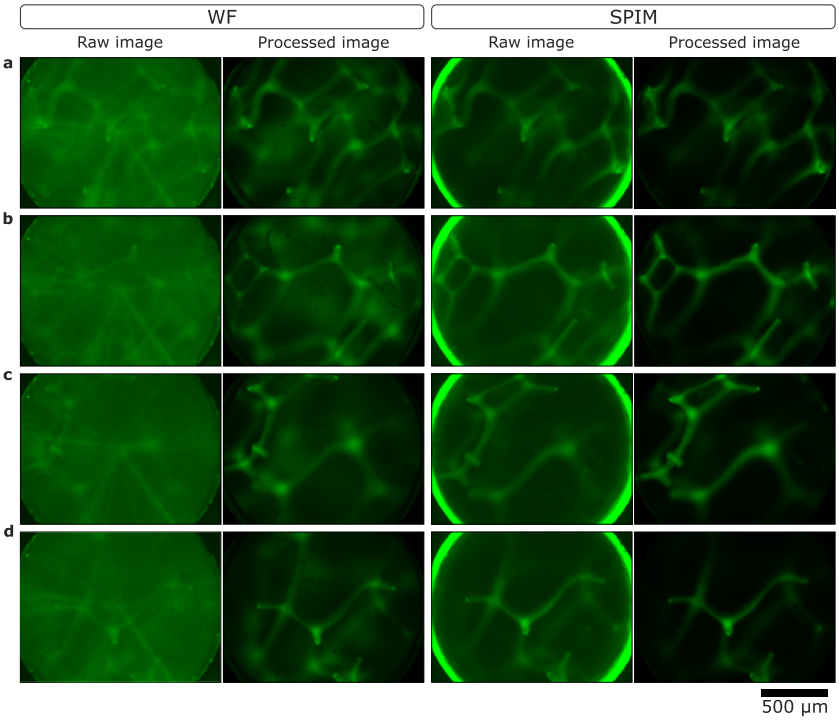


**FIG. 4.** Widefield and SPIM images showing improved contrast and a reduction of out-of-focus features. (a)–(d) Corresponding FOVs acquired in WF and SPIM modality. Raw images demonstrate the strong fiber fluorescence that is present in the WF case. The clear ring present in the raw SPIM images is backscattered fiber fluorescence, as a result of pumping the excitation light down these cores. Processed images (see Methods) demonstrate qualitatively improved imaging using the SPIM probe. Evaluation of these images is shown in Fig. 5.

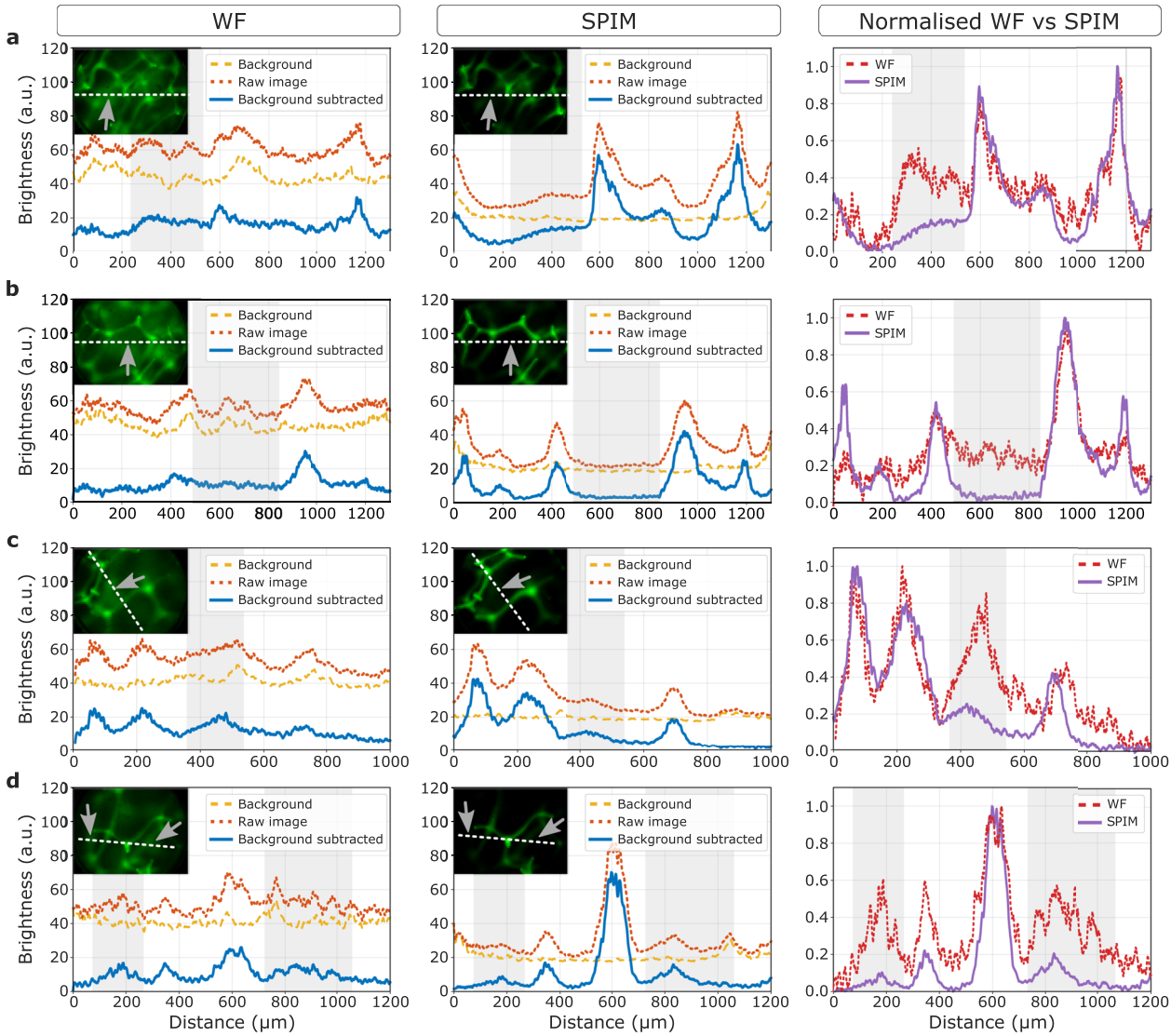


**FIG. 5.** Evaluation of WF and SPIM images. (a)–(d) Line profiles across images shown in Fig. 4 demonstrate reduced out-of-focus background and improved contrast of SPIM. Insets show image and line plotted (dashed white line). (Left) and (middle) WF and SPIM image, respectively, with measured background (yellow dashed line), raw image (orange dotted line), and image with subtracted background (blue solid line). (right) Normalized WF (red dashed line) and SPIM (purple solid line) line profiles after background subtraction. Gray fill in each plot corresponds to areas shown by gray arrows, where background features are less visible in SPIM. Brightness and contrast of inset images have been adjusted for visibility. Line profiles were taken on raw data and then smoothed using a Savitzky–Golay filter (window = 29, polynomial order = 2).

### D. Imaging: Evaluation with a phantom and demonstration in *ex vivo* human lungs

Representative examples of a tissue phantom, imaged in both WF and SPIM modality (see Methods), are shown in Fig. 4. More examples can be seen in supplementary material, Fig. 3. Raw WF and SPIM images of each FOV are given, to demonstrate the significant fluorescence background originating from the PMMA CFB cores. In the WF case, it can be seen that this fluorescence background is severe and obscures many of the image features. Subtraction of the background improves visibility of image features, but does not minimize the presence of out-of-focus features within the FOV.

Quantitative evaluation of the tissue phantom images is shown in Fig. 5. Each inset (a)–(d) contains three plots: (i) The left plot represents a WF image. (ii) The middle plot represents a SPIM image of the same FOV. In these plots, line profiles of the measured background are shown as yellow dashed lines, raw images as orange dotted lines, and images with background subtracted as blue solid lines. (iii) The right plot compares WF (red dotted line) and SPIM (purple solid line) after background subtraction and normalization. In Figs. 5(a) and 5(b), random pairs of WF and SPIM images were selected, and horizontal line profiles were drawn through the FOV. Several observations can be noted. (i) The measured

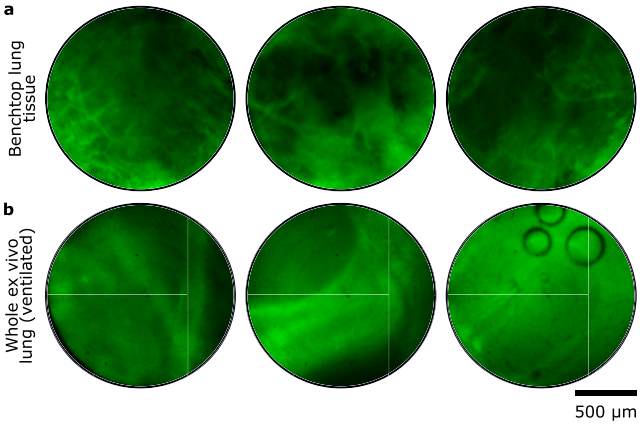


**FIG. 6.** Representative examples of *ex vivo* human lung tissue. (a) Lung tissue sample imaged on the benchtop using the SPIM probe at 5 fps. (b) Mechanically ventilated, whole, *ex vivo* human lungs, imaged through the SPIM probe at 7 fps. The alveolar space is reached via a transbronchial pass. See supplementary material, videos 2 (Multimedia view) and 3 (Multimedia view). Images and videos have been processed as described in Methods.

background in the WF case is higher than that in the SPIM case (yellow dashed lines). Furthermore, the background within the SPIM FOV was comparable to the measured camera background itself, except for an uptick in background within ~100 $\mu$m of the excitation ring of cores, as can be seen at the extreme ends of the line profiles. (ii) Out-of-focus features, indicated by gray arrows in images and gray fill in plots, are diminished in the SPIM case. This is particularly clear when comparing normalized WF and SPIM line profiles (red dashed line and purple solid line, respectively). (iii) Signal-to-noise is improved in the SPIM case, in comparison to the WF case. In Figs. 5(c) and 5(d), line profiles within the FOV were preferentially chosen to include out-of-focus features, which are clearly present in the WF image and minimized in the SPIM image. Again, gray arrows indicate out-of-focus features in the inset images, which are represented in the gray fill regions of the plots. From these results, it is clear that the SPIM probe results in higher contrast images, with a reduction in out-of-focus image features.

Finally, as a proof-of-concept demonstrator, we acquired images from human lung tissue. This was done with both excised lung tissue and whole, ventilated *ex vivo* lungs, whereby the SPIM probe was delivered into the alveolar space (see Methods). Figure 6 shows various frames from video capture of excised tissue imaged on the benchtop [Fig. 6(a), Multimedia view] and of whole lungs imaged via the trachea [Fig. 6(b), Multimedia view] (see also supplementary material, videos 2 and 3). Without the use of exogenous fluorophores, we were able to visualize alveolar tissue in real-time (either 5 or 7 fps) using the SPIM probe platform. Due to the dynamic nature of the experiment, it was not possible to collect comparable FOVs in WF and SPIM modality. A full, quantitative, comparative study of the SPIM probe with a WF system is out of scope of this work, but will be pursued in the future.

## III. MATERIALS AND METHODS

### A. PMMA CFB

In this work, we used a PMMA CFB (MCL-1500-1.75, Asahi Kasei Corporation). The CFB has a diameter of 1.5 mm and 13 000 cores, each with a diameter of ~10.5 $\mu$m. The cores are PMMA, and the cladding is a fluorinated polymer, with refractive indices of 1.49 and 1.4, respectively (as stated by the manufacturer and confirmed with refracted near-field measurement). The core pitch (distance between core center and nearest neighbor core center) is ~12 $\mu$m [see SEM image in Fig. 2(a)], and the cores have a numerical aperture (NA) of 0.5. The CFB is packaged with a polyethylene jacket, which results in a full outer diameter of 1.75 mm.

### B. End-cap fabrication: Ultrafast laser inscription and chemical etching

Femtosecond laser writing was performed using a Menlo Systems BlueCut fiber laser (Menlo Systems GmbH) that delivers 350 fs laser pulses at a central wavelength of 1030 nm. A pulse repetition rate of 250 kHz and a pulse energy of 250 nJ were used. The inscription speed was 3 mm/s, thus obtaining 83.3 pulses/$\mu$m. To obtain the highest selectivity in the subsequent chemical etching of the structures, the polarization was set linear and perpendicular to the intended etching direction.[39] As the end-cap inscription is circular, the polarization was dynamically controlled during laser inscription, by rotating a $\lambda/2$ waveplate. The laser pulses were tightly focused into the 1 mm thick, high purity fused silica glass (UV Grade Corning 7980 0F), using a 0.4 NA aspheric lens (A110TM-B, Thorlabs). The substrate was translated through the laser focus using a motorized nano-resolution XYZ crossed roller bearing stage (Alio Industries), and the stage motion was controlled using ACSPL+ programming language. Figure 2(d) shows a micrograph of the fused silica substrate after ULI.

In the subsequent etching process, the inscribed fused silica glass was immersed for 3 h in a magnetically stirred etching solution of KOH diluted with deionized water (8 mol/l, 85 °C). The etching time was determined empirically, to facilitate easy release of the two parts forming the end-cap, without over-etching. The two parts were individually removed and rinsed with deionized water [see Figs. 2(e) and 2(f)].

The top part of the end-cap was silver-coated on the surface shown in Fig. 2(b) by e-beam deposition (MiniLab 080 System, Moorfield Nanotechnology Limited). The coating thickness was 90 ± 10 nm.

Before assembling the end-cap to the fiber, the two ends of the CFB were polished according to the following procedure: 30 s (1000–grit sandpaper), 1 min (4000–grit sandpaper), 2 min (12 $\mu$m of grit size lapping film), 3 min (5 $\mu$m grade lapping film), 4 min (3 $\mu$m grade lapping film), and 5 min (1 $\mu$m grade lapping film).

Finally, both parts of the end-cap were assembled using manual translations stages and glued with UV-curable optical adhesive (NOA 61, Norland) [see Fig. 2(g)]. Similarly, the end-cap was glued (NOA 68, Norland) to the polished distal end of a 1.5 m length of the fiber [see Fig. 2(h)], and a flexible heat-shrink tube was attached for protection during experiments.

### C. Spectral measurements

Figure 3(a) shows the system used for measuring the fluorescence emission of fiber cores. The output of a fiber-coupled 485 nm laser (LDH-D-C-485 with PDL 800-D driver, PicoQuant) was collimated and coupled into a single core at the proximal end of the CFB via lenses $L_1$ and $L_2$, which were selected so that the incident laser spot would not over-fill the core. At the distal end of the fiber, a camera (DCC1645C, Thorlabs) was used to provide feedback for positioning the fiber with respect to the proximal end laser spot, such that the pump light was incident on the core and not the cladding. The laser was operated in CW mode, and the power was measured to be 200 $\mu$W. Backscattered fluorescence induced in the core was then coupled via a multimode fiber (M42L01, Thorlabs) to a spectrometer (QE-Pro VIS, Ocean Optics now Ocean Insight) for readout.

### D. Ray-trace simulations

Ray-trace simulations were carried out to characterize both the selective plane profile and the intensity drop-off after the fiber in the direction of its axial axis (Z-axis). Zemax OpticStudio software (version 22.2) was used with Matlab (version R2022a Update 1, The MathWorks Inc.) as the application programming interface (API). Standalone mode was the program mode used for the connection between Matlab and Zemax OpticStudio. For the simulations, non-sequential ray-tracing mode was employed. Both end-cap parts were included as CAD parts, and each simulated core was modeled as a source point, with an illumination angle cone defined by the NA of the fiber. A nominal 1 mW was launched at the proximal end of the fiber, with a total of 1000 rays per core. 485 nm wavelength was employed. Both the 3D model of the end-cap and simulations are included as supplementary material.

The intensity distribution in the 2D detector plane [Fig. 3(b) bottom left] was obtained in the SPIM case, using the end-cap with a 70 $\mu$m thick ring-illumination (2337 cores simulated, 100%), and in the WF case, using a bare fiber with flood-illumination (10 000 cores simulated, placed randomly, 76.92%). The 2D detector plane was oriented as shown in the top of Fig. 3(b), i.e., containing the axial axis of the fiber, initiating at the fiber end face, and with dimensions of 1.35 and 4 mm in the Y and Z axes (1001 × 1001 pixels), respectively. The averaged intensity as a function of propagation distance [Fig. 3(b) bottom right], for both SPIM and WF, was extracted from the intensity distribution in the 2D detector plane, as $I(z) = (L_y)^{-1} \int_y I(y,z) \cdot dy$, with $L_y$ = 1.35 mm.

It should be noted that neither the attenuation of the PMMA fiber nor its scattering were taken into account in the simulations. The autofluorescence of the PMMA fiber, when excited at the working wavelength, has also not been taken into account.

### E. Epifluorescence microscope setup

A dual-illumination epifluorescence microscope was constructed, shown schematically in Fig. 1(e). The microscope allows for easy switching between optical paths via a rotatable dichroic mirror, leading to either ring-illumination or flood-illumination of the proximal end of the fiber for SPIM imaging or WF imaging, respectively. In either arrangement, excitation was provided by a 485 nm laser [Fig. 1(e) (L)] (LDH-D-C-485 with PDL 800-D driver, PicoQuant), operated in CW mode.

For SPIM imaging, the following excitation path was used. A lens ($L_1$) (C230TMD, Thorlabs) was used to collimate the output of a single-mode patchcord (P5-405-FC-2, Thorlabs) connected to the laser. The collimated beam was then expanded using a 5× beam expander (BE) (GBE05-A, Thorlabs) and passed through an excitation filter (Ex) (FITC-Ex01-Clin-25, Semrock). The light was then reflected via an aluminum mirror (M) (PF10-03-G01, Thorlabs) and passed through an axicon lens with a 9° angle of divergence ($L_{ax}$) (AX122-A, Thorlabs). An image plane (Im.) of the ring-shaped beam was then created by a lens ($L_2$) (LA1131-A-ML, Thorlabs). An optical mask (Mask) positioned in the image plane was used to block any stray light in the center of the ring-shaped beam. This image plane was relay imaged onto the proximal end of the CFB using a second lens ($L_3$) (LA1131-A-ML, Thorlabs) and a 4× objective lens ($L_{obj}$) (RMS4X, Olympus) via the dichroic (DM) (FITC-Di01-Clin-25 × 36, Semrock). The optical mask was fabricated via ULI-CE on a 1 mm thick fused silica substrate (UV Grade Corning 7980 0F), onto which a ∅ 1.36 mm central circle was silver-coated to opacity. The axicon and lenses were selected together, to create a ring of illumination on the CFB, with a 1.5 mm outer diameter and 70 $\mu$m inwardly protruding thickness. Thus, excitation light was only coupled to cores capped by the end-cap mirror.

For WF imaging, the following excitation path was used. Excitation light from a single-mode patchcord (P5-405-FC-2, Thorlabs) connected to the laser was collimated via a tube lens ($L_4$) (TTL-200-A, Thorlabs) and passed through an excitation filter (Ex) (FITC-Ex01-Clin-25, Semrock). The dichroic mirror (DM) (FITC-Di01-Clin-25 × 36, Semrock) was angled to redirect this light through the objective lens ($L_{obj}$) (RMSRMS4X, Olympus) onto the proximal end of the CFB. The relative position of the patchcord output and the tube lens was then adjusted, to massively defocus the laser spot incident on the CFB, until even illumination of the central column of the cores was obtained.

In either SPIM or WF mode, fluorescence images were acquired through the same objective lens and dichroic mirror. Subsequently, after including an emission filter ($L_{Em}$) (FITC-LP01-Clin-25, Semrock) and a tube lens ($L_5$) (TTL200-A, Thorlabs), the images were captured by a camera with a monochrome CMOS sensor (C) (GS3-U3-32S4M-C, FLIR).

### F. Tissue phantom imaging: Protocol

Image characterization was performed using a polymer sponge (yellow dish sponge), which has a loosely-packed strand structure. The distal end of the CFB and the tissue phantom were secured to separate three-axis translation stages (MBT616D, Thorlabs), providing a way to precisely locate a FOV and maintain it through sequential image acquisitions. In SPIM/WF mode, the power of the 485 nm laser was set to 1.6 mW, as measured between the objective and the proximal fiber face. With the distal end of the CFB retracted from the tissue phantom and non-reflective black card placed between the CFB and the phantom, a background image was taken. The distal end of the CFB was then translated to make contact with the tissue phantom and another image was acquired. Without moving the CFB or the tissue phantom, the fibered laser was coupled to the WF/SPIM illumination path, and the dichroic mirror was rotated to flood/ring illuminate the proximal end of the CFB. The laser output power was adjusted, if needed, to achieve 1.6 mW, measured between the objective and the proximal fiber face, and an

image of the phantom was acquired. The CFB was then retracted, black card was used to block the extended light path between the CFB and the phantom, and a background image was acquired. This process thus resulted in a dataset containing four images: a FOV image and a background image pair in both SPIM and WF modalities. Images were taken with a 200 ms exposure time and a detector gain of 15 dB.

### G. Tissue phantom imaging: Line profile analysis

Line profiles were taken on each of the four images in a dataset using ImageJ.[42] Any displacement of the relative position of the fiber within the image frame was accounted for, to ensure that lines were drawn through corresponding image scenes without lateral translation. Any datasets where the phantom itself had moved during data collection were discarded. The data were plotted after being smoothed by a Savitzky–Golay filter,[43] with a window-length of 29 and a polynomial order of 2. The filter parameters were determined empirically, such that the fiber core pattern present in the data was minimized, while preserving the apparent relative signal-to-noise ratio between WF and SPIM data.

### H. Lung imaging

Images of lung tissue were taken either from a sample of human lungs or whole lungs. For the former, a few centimeters of tissue was excised from a lower lobe and placed in a dish. The tissue was punctured as necessary, to gain access to the alveolar space. Images were acquired at 200 ms exposure (5 fps), with a detector gain of 15 dB, in sets of 200 images. Fiber background images were taken before and after each 200 image set. For the latter, a pair of whole *ex vivo* human lungs were mechanically ventilated (Dräger Savina 300) by securing the ventilator endotracheal tube within the trachea. The SPIM probe was delivered via the endotracheal tube and passed into various regions of the distal lungs by an operator, using real-time SPIM probe platform imaging for guidance. Images were acquired at 150 ms exposure (7 fps), with a detector gain of 15 dB, in sets of 1000 images. Fiber background images were taken before and after each 1000 image set.

### I. Image processing

The data consist of images of circular fibers, captured in a rectangular format, such that there is clipping of the fiber diameter in the horizontal and vertical directions (see Fig. 4). The subset of fiber cores used for excitation in the SPIM case, as well as the corresponding cores in the WF case, were excluded from the analysis below. The array of remaining cores, the imaging cores, are referred to collectively as the fiber FOV below. All images were acquired with a monochrome sensor, 8-bit depth in each pixel ($L = 8$). The mathematical notation of each image is shown in Eq. (1).

$$\mathbf{I_\alpha} \in \mathbb{Z}^{M\times N} \;:\; I_\alpha(x,y) \in [0, 2^L - 1] \subset \mathbb{Z}_0^+, \quad \forall\ \{x \in X,\ y \in Y\}, \tag{1}$$

where $\alpha$ can refer to the raw image ($\alpha = r$), background image ($\alpha = b$), subtracted image ($\alpha = s$), contrast-optimized image ($\alpha = c$), or filtered image ($\alpha = f$). Similarly, $X = [1, N] \subset \mathbb{Z}$, and $Y = [1, M] \subset \mathbb{Z}$, where $N$ and $M$ refer to the width and height in the pixels of the image, respectively. In this case, $N = 2048$ and $M = 1536$.

For visualization of image data contained in Figs. 4 and 6, image processing was carried out as follows:. The acquired background ($\mathbf{I_b}$) was subtracted from the corresponding raw image ($\mathbf{I_r}$), obtaining $\mathbf{I_s}$ [Eq. (2)],

$$\mathbf{I_s} = \mathbf{I_r} - \mathbf{I_b}. \tag{2}$$

The contrast within the fiber FOV in $\mathbf{I_s}$ was then enhanced by performing a linear transform of the pixel values, while maintaining the "zero" value, to obtain $\mathbf{I_c}$. To determine this transform, we established a "useful" maximum pixel value contained within the fiber FOV, $l_{adj}$, which we later used to adjust the image, while ignoring dead or anomalously high-valued pixels. For the calculation of $l_{adj}$, a histogram of the fiber FOV within $\mathbf{I_s}$ defined as $\mathbf{H_s}$, was taken. Then, defining $l_c$ as the modal value within $\mathbf{H_s}$, we determined $l_{adj}$ as the maximum pixel value that satisfies $H_s(l_{adj}) \geq 0.01 \cdot H_s(l_c)$.

We then apply a linear transform on $\mathbf{I_s}$ to obtain $\mathbf{I_c}$ according to Eq. (3),

$$I_c(x,y) = \begin{cases} I_s(x,y), & I_s(x,y) < (I_s)_{\min}. \\ \dfrac{2^L - 1 - (I_s)_{\min}}{l_{adj} - (I_s)_{\min}}\left[I_s(x,y) - (I_s)_{\min}\right] + (I_s)_{\min}, & (I_s)_{\min} \leq I_s(x,y) \leq l_{adj}. \\ 2^L - 1, & I_s(x,y) > l_{adj}. \end{cases} \tag{3}$$

This way, the "zero" value in the fiber FOV is maintained, while maximizing contrast enhancement of useful information in the image.

Finally, to reduce the prominence of the core pattern in the displayed image, a two-dimensional Weierstrass transform (Gaussian blur with standard deviation $\sigma = 4$) was applied,[44] resulting in image ($\mathbf{I_f}$). Figures 4 and 6 contain processed images ($\mathbf{I_f}$).

## IV. DISCUSSION AND CONCLUSION

In this work, we developed a fused silica end-cap, to enable SPIM through a fiber, while maintaining a form factor conducive to endoscopic deployment. Our SPIM platform has two key strengths. First, it avoids the effect of PMMA fiber core fluorescence (when pumped with blue light), by using separate excitation and imaging cores. Second, it reduces the appearance of the out-of-focus features in an imaged sample, which would otherwise decrease image contrast.

As measured, the fluorescence emitted from cores of a PMMA CFB is undesirable. The fluorescence spectrum [Fig. 3(a)] reveals several strong emission peaks within the typical endogenous fluorescence imaging window (~500–600 nm). Careful selection of filters could result in removal of these peaks from the images, but with

a severe loss of signal. Moreover, regions of minima between the measured emission peaks are still significantly higher than the measured emission from the silica fiber within the same wavelength range. It is important to note the effect of this fiber fluorescence in images. When used in WF mode, the fluorescence emission of the PMMA CFB can be thought of as a DC component in the acquired images. Removing this background is trivial, as was done in Fig. 4. However, the fluorescence background adds noise to the image, which is not removed through background subtraction, and can be seen in Fig. 5. Thus, using separate cores for excitation and collection is a superior approach for improving the usability of PMMA CFBs. Furthermore, due to the unusually large diameter of polymer fibers, it is possible to subdivide the core array in this manner, without significantly compromising the FOV. We allocated ~2300 cores to the excitation path, leaving a sizable 1.36 mm diameter imaging window. This is significantly larger than many commercial silica CFBs, for example the Confocal Miniprobes™ range of imaging fibers with FOVs in the range of 240–600 $\mu$m (Mauna Kea Technologies, Paris, France).

Simulation data show our SPIM end-cap results in good confinement of excitation light in the end-cap front recess [Fig. 3(b)]. Specifically, when integrated over the 170 $\mu$m corresponding to the depth of the front recess of the end-cap, the power is ~2.97 times greater than that in the corresponding propagation distance in the WF case. Furthermore, an intensity decay of 20 dB is achieved in just ~0.7 mm, enabling the optical sectioning capabilities seen here. These results bear out in our comparison of image feature contrast in equivalent WF and SPIM FOVs of a tissue phantom. We selected line profiles through these images and revealed that, in addition to a reduction in noise as discussed above, the prominence of out-of-focus features is decreased in SPIM images (Fig. 5). Additionally, using an *ex vivo* human lung model (Fig. 6, Multimedia view), we demonstrated that the SPIM probe platform operates with sufficient excitation and collection efficiency, to visualize tissue fluorescence *in situ,* without the use of any exogenous fluorophores.

Underpinning several of our choices in this work was the goal of achieving a high performance fiber-based imaging probe without high cost. Silica CFBs are available directly from manufacturers, such as Fujikura,[45] for ~$100s USD per meter (FIGH-30-650S, $575 USD per meter). Most of the fabrication steps of the SPIM probe are scalable. Multiple end-caps can be inscribed in a single glass substrate, decreasing both fabrication time and cost. Further reduction in inscription time could be achieved by adopting laser beam shaping techniques.[46] Similarly, etching and silver coating processes can be performed in batches. With appropriate scaling, the manufacturing costs of the end-cap can be considered practically negligible compared to the price of PMMA fiber (~$30 USD per meter[47]). It is, therefore, conceivable to consider, even taking into account future regulatory costs associated with translation of a device to the clinic, that such a polymer SPIM probe holds potential as a low-cost, single-use, disposable device. As such, we have avoided the need to overcome challenges related to sterilization processes, which may add substantial cost or be impossible to perform. For example, while the fused silica end-cap could tolerate an autoclave procedure without issue, the PMMA fiber is irreversibly damaged by temperatures above 60–70 °C and would not survive the autoclaving process. PMMA is routinely used within microfluidics contexts and sterilization with ethylene oxide[48] could be a viable pathway toward re-usability, although this is beyond the scope of the present work.

Finally, we identify several potential areas of improvement. We observed trapped air during *ex vivo* lung imaging (Fig. 6 bottom right, Multimedia view). Although the air could be dispersed with gentle agitation of the SPIM probe from outside of the lungs, small notches integrated in the perimeter of the end-cap design could alleviate this issue without much disruption to the excitation path. Some imaging targets/tissues may benefit from a tighter illumination plane and, therefore, higher fidelity optical sectioning. This could be achieved by reducing the thickness of the ring of cores used for excitation, provided sufficient illumination is preserved overall. Along similar lines, dynamically addressing separate, thin rings of cores of different diameters, corresponding to a change in the depth of the illumination plane, could allow us to achieve Z-stacking of the FOV (with a reduced acquisition time, compared with the current SPIM arrangement).

To summarize, our fused silica end-cap offers the possibility to perform SPIM through a single polymer imaging fiber. We believe that our technique has the potential to be an enabling technology for cost-effective microendoscopes in many applications, including FBEμ of the respiratory system.

## SUPPLEMENTARY MATERIAL

See the supplementary material for further images of the tissue phantom, as well as measurements and simulations of the MCL-1500-1.75 core crosstalk imaging fiber. A 3D animation of the end-cap assembly on the fiber is also included, as well as videos performed with the SPIM end-cap on *ex vivo* human lung tissue.

## ACKNOWLEDGMENTS

We sincerely thank the relatives of the lung donors and all those involved in enabling the use of these organs in the research. We would like to thank Neil Ross, Jamie Slattery, and David MacLachlan for technical expertise and assistance in relation to the fabrication of the end-cap. We thank Ahad Abdalla and Tom Quinn for their assistance with lung tissue. This work was supported by the MICIU, AEI and FEDER funds of European Commission (Grant No. PID2019-107270RB-C21), the MECD of Spain (Grant No. FPU2018/02797), the MIU of Spain (Grant No. EST19/00956), and the UK Research and Innovation EPSRC (Grant Nos. EP/P027415/1, EP/T020903/1, EP/S000410/1, and EP/S025987/1). We also acknowledge the use of a number of packages for scientific computing in Python.[43,49,50] Finally, we thank Heriot-Watt University for providing open access publication funds.

## AUTHOR DECLARATIONS

### Conflict of Interest

A patent application related to the SPIM end-cap was filed on 21 April 2022 to the UK Intellectual Property Office. PR.-V., C.A.R., M.G.T., R.R.T., and H.E.P are named inventors on this patent. The

patent application number is GB2205826.7. The other co-authors declare no competing interests.

## Ethics Approval

Tissue samples were obtained from lungs deemed non-transplantable and where families had consented to their use in medical research. All experiments were carried out following appropriate approvals. REC ref: LO-16-1883.

## Author Contributions

P.R.-V. and H.E.P. contributed equally to this work.

**Pablo Roldán-Varona**: Data curation (equal); Formal analysis (equal); Investigation (equal); Methodology (equal); Software (equal); Validation (equal); Visualization (equal); Writing – original draft (equal); Writing – review & editing (equal). **Calum A. Ross**: Investigation (equal); Software (supporting); Supervision (supporting); Validation (equal); Writing – review & editing (equal). **Luis Rodríguez-Cobo**: Supervision (equal); Writing – review & editing (equal). **José Miguel López-Higuera**: Supervision (equal). **Erin Gaughan**: Investigation (supporting); Writing – review & editing (equal). **Kevin Dhaliwal**: Investigation (supporting); Resources (supporting); Validation (equal); Writing – review & editing (equal). **Michael G. Tanner**: Conceptualization (equal); Funding acquisition (equal); Investigation (equal); Project administration (equal); Supervision (equal); Writing – review & editing (equal). **Robert R. Thomson**: Conceptualization (equal); Funding acquisition (lead); Project administration (lead); Resources (lead); Supervision (lead); Writing – review & editing (equal). **Helen E. Parker**: Data curation (equal); Formal analysis (equal); Investigation (equal); Methodology (equal); Software (equal); Validation (equal); Visualization (equal); Writing – original draft (equal); Writing – review & editing (equal).

## DATA AVAILABILITY

The data that support the findings of this study are openly available in the Heriot-Watt University repository at https://doi.org/10.17861/31f319c0-66eb-41b0-a586-6f2480c85a47.

## REFERENCES


[1] B. A. Flusberg, E. D. Cocker, W. Piyawattanametha, J. C. Jung, E. L. M. Cheung, and M. J. Schnitzer, "Fiber-optic fluorescence imaging," Nat. Methods **2**, 941–950 (2005).

[2] A. Perperidis, K. Dhaliwal, S. McLaughlin, and T. Vercauteren, "Image computing for fibre-bundle endomicroscopy: A review," Med. Image Anal. **62**, 101620 (2020).

[3] G. A. Sonn, S.-N. E. Jones, T. V. Tarin, C. B. Du, K. E. Mach, K. C. Jensen, and J. C. Liao, "Optical biopsy of human bladder neoplasia with in vivo confocal laser endomicroscopy," J. Urol. **182**, 1299–1305 (2009).

[4] J.-J. Liu, M. J. Droller, and J. C. Liao, "New optical imaging technologies for bladder cancer: Considerations and perspectives," J. Urol. **188**, 361–368 (2012).

[5] A. L. Polglase, W. J. McLaren, S. A. Skinner, R. Kiesslich, M. F. Neurath, and P. M. Delaney, "A fluorescence confocal endomicroscope for in vivo microscopy of the upper- and the lower-GI tract," Gastrointest. Endoscopy **62**, 686–695 (2005).

[6] A. Fugazza, F. Gaiani, M. C. Carra, F. Brunetti, M. Lévy, I. Sobhani, D. Azoulay, F. Catena, G. L. de'Angelis, and N. de'Angelis, "Confocal laser endomicroscopy in gastrointestinal and pancreatobiliary diseases: A systematic review and meta-analysis," BioMed Res. Int. **2016**, 4638683 (2016).

[7] S. G. Krishna, P. A. Hart, J. M. DeWitt, C. J. DiMaio, P. Kongkam, B. Napoleon, M. O. Othman, D. M. Yew Tan, S. G. Strobel, P. P. Stanich, A. Patel, A. K. Luthra, M. Q. Chan, A. M. Blaszczak, D. Lee, S. El-Dika, S. T. McCarthy, J. P. Walker, C. A. Arnold, K. Porter, and D. L. Conwell, "EUS-guided confocal laser endomicroscopy: Prediction of dysplasia in intraductal papillary mucinous neoplasms (with video)," Gastrointest. Endoscopy **91**, 551–563.e5 (2020).

[8] T. Quang, R. A. Schwarz, S. M. Dawsey, M. C. Tan, K. Patel, X. Yu, G. Wang, F. Zhang, H. Xu, S. Anandasabapathy, and R. Richards-Kortum, "A tablet-interfaced high-resolution microendoscope with automated image interpretation for real-time evaluation of esophageal squamous cell neoplasia," Gastrointest. Endoscopy **84**, 834–841 (2016).

[9] M. C. Pierce, P. M. Vila, A. D. Polydorides, R. Richards-Kortum, and S. Anandasabapathy, "Low-cost endomicroscopy in the esophagus and colon," Am. J. Gastroenterol. **106**, 1722–1724 (2011).

[10] P. Su, Y. Liu, S. Lin, K. Xiao, P. Chen, S. An, J. He, and Y. Bai, "Efficacy of confocal laser endomicroscopy for discriminating colorectal neoplasms from non-neoplasms: A systematic review and meta-analysis," Colorectal Dis. **15**, e1–e12 (2013).

[11] B. Mills, A. Megia-Fernandez, D. Norberg, S. Duncan, A. Marshall, A. R. Akram, T. Quinn, I. Young, A. M. Bruce, E. Scholefield, G. O. S. Williams, N. Krstajić, T. R. Choudhary, H. E. Parker, M. G. Tanner, K. Harrington, H. A. C. Wood, T. A. Birks, J. C. Knight, C. Haslett, K. Dhaliwal, M. Bradley, M. Ucuncu, and J. M. Stone, "Molecular detection of gram-positive bacteria in the human lung through an optical fiber–based endoscope," Eur. J. Nucl. Med. Mol. Imaging **48**, 800–807 (2020).

[12] A. S. Wellikoff, R. C. Holladay, G. H. Downie, C. S. Chaudoir, L. Brandi, and E. A. Turbat-Herrera, "Comparison of in vivo probe-based confocal laser endomicroscopy with histopathology in lung cancer: A move toward optical biopsy," Respirology **20**, 967–974 (2015).

[13] L. Thiberville, M. Salaün, S. Lachkar, S. Dominique, S. Moreno-Swirc, C. Vever-Bizet, and G. Bourg-Heckly, "Human *in vivo* fluorescence microimaging of the alveolar ducts and sacs during bronchoscopy," Eur. Respir. J. **33**, 974–985 (2009).

[14] B. Hirschowitz, "Endoscopic examination of the stomach and duodenal cap with the fiberscope," Lancet **277**, 1074–1078 (1961).

[15] A. Perperidis, H. E. Parker, A. Karam-Eldaly, Y. Altmann, K. Dhaliwal, R. R. Thomson, M. G. Tanner, and S. McLaughlin, "Characterization and modelling of inter-core coupling in coherent fiber bundles," Opt. Express **25**, 11932–11953 (2017).

[16] H. E. Parker, A. Perperidis, J. M. Stone, K. Dhaliwal, and M. G. Tanner, "Core crosstalk in ordered imaging fiber bundles," Opt. Lett. **45**, 6490–6493 (2020).

[17] N. Ortega-Quijano, F. Fanjul-Vélez, and J. L. Arce-Diego, "Optical crosstalk influence in fiber imaging endoscopes design," Opt. Commun. **283**, 633–638 (2010).

[18] J. M. Stone, H. A. C. Wood, K. Harrington, and T. A. Birks, "Low index contrast imaging fibers," Opt. Lett. **42**, 1484 (2017).

[19] N. Krstajić, B. Mills, I. Murray, A. Marshall, D. Norberg, T. H. Craven, P. Emanuel, T. R. Choudhary, G. O. S. Williams, E. Scholefield, A. R. Akram, A. Davie, N. Hirani, A. Bruce, A. Moore, M. Bradley, and K. Dhaliwal, "Low-cost high sensitivity pulsed endomicroscopy to visualize tricolor optical signatures," J. Biomed. Opt. **23**, 1–12 (2018).

[20] X. Hong, V. K. Nagarajan, D. H. Mugler, and B. Yu, "Smartphone microendoscopy for high resolution fluorescence imaging," J. Innovative Opt. Health Sci. **09**, 1650046 (2016).

[21] H. E. Parker, J. M. Stone, A. D. L. Marshall, T. R. Choudhary, R. R. Thomson, K. Dhaliwal, and M. G. Tanner, "Fibre-based spectral ratio endomicroscopy for contrast enhancement of bacterial imaging and pulmonary autofluorescence," Biomed. Opt. Express **10**, 1856–1869 (2019).

[22] A. F. Gmitro and D. Aziz, "Confocal microscopy through a fiber-optic imaging bundle," Opt. Lett. **18**, 565 (1993).

[23]F. Jean, G. Bourg-Heckly, and B. Viellerobe, "Fibered confocal spectroscopy and multicolor imaging system for in vivo fluorescence analysis," Opt. Express **15**, 4008 (2007).
[24]M. Hughes and G.-Z. Yang, "Line-scanning fiber bundle endomicroscopy with a virtual detector slit," Biomed. Opt. Express **7**, 2257–2268 (2016).
[25]H. Zhang, Z. He, Z. Jin, Q. Yan, P. Wang, and X. Ye, "The development and clinical application of microscopic endoscopy for in vivo optical biopsies: Endocytoscopy and confocal laser endomicroscopy," Photodiagn. Photodyn. Ther. **38**, 102826 (2022).
[26]M. H. Koucky and M. C. Pierce, "Axial response of high-resolution microendoscopy in scattering media," Biomed. Opt. Express **4**, 2247 (2013).
[27]E. H. K. Stelzer, F. Strobl, B.-J. Chang, F. Preusser, S. Preibisch, K. McDole, and R. Fiolka, "Light sheet fluorescence microscopy," Nat. Rev. Methods Primers **1**, 73 (2021).
[28]C. J. Engelbrecht, F. Voigt, and F. Helmchen, "Miniaturized selective plane illumination microscopy for high-contrast *in vivo* fluorescence imaging," Opt. Lett. **35**, 1413–1415 (2010).
[29]M. Murayama, E. Pérez-Garci, H.-R. Lüscher, and M. E. Larkum, "Fiberoptic system for recording dendritic calcium signals in layer 5 neocortical pyramidal cells in freely moving rats," J. Neurophysiol. **98**, 1791–1805 (2007).
[30]W. D. Sacher, F.-D. Chen, H. Moradi-Chameh, P. Shah, I. Felts Almog, Y. Youngho Jun, T. Hu, J. Jeong, A. M. Lozano, T. A. Valiante, L. C. Moreaux, J. K. Poon, M. L. Roukes, X. Luo, A. Fomenko, T. Lordello, X. Liu, J. N. Straguzzi, T. M. Fowler, and P. Lo, "Implantable photonic neural probes for light-sheet fluorescence brain imaging," Neurophotonics **8**, 025003 (2021).
[31]N. C. Lin, X. Zhao, S. Hassan, A. Raghuram, A. Veeraraghavan, and J. T. Robinson, "Implantable integrated photonic probe for light sheet brain imaging in vivo," in *Biophotonics Congress 2021* (OSA, 2021).
[32]D. Choudhury, J. R. Macdonald, and A. K. Kar, "Ultrafast laser inscription: Perspectives on future integrated applications," Laser Photonics Rev. **8**, 827–846 (2014).
[33]T. Gissibl, S. Thiele, A. Herkommer, and H. Giessen, "Two-photon direct laser writing of ultracompact multi-lens objectives," Nat. Photonics **10**, 554–560 (2016).
[34]Y. Hu, S. Rao, S. Wu, P. Wei, W. Qiu, D. Wu, B. Xu, J. Ni, L. Yang, J. Li, J. Chu, and K. Sugioka, "All-glass 3D optofluidic microchip with built-in tunable microlens fabricated by femtosecond laser-assisted etching," Adv. Opt. Mater. **6**, 1701299 (2018).
[35]D. Wu, J. Xu, L.-G. Niu, S.-Z. Wu, K. Midorikawa, and K. Sugioka, "In-channel integration of designable microoptical devices using flat scaffold-supported femtosecond-laser microfabrication for coupling-free optofluidic cell counting," Light: Sci. Appl. **4**, e228 (2015).
[36]R. R. Gattass and E. Mazur, "Femtosecond laser micromachining in transparent materials," Nat. Photonics **2**, 219–225 (2008).
[37]C. B. Schaffer, A. Brodeur, and E. Mazur, "Laser-induced breakdown and damage in bulk transparent materials induced by tightly focused femtosecond laser pulses," Meas. Sci. Technol. **12**, 1784–1794 (2001).
[38]B. C. Stuart, M. D. Feit, S. Herman, A. M. Rubenchik, B. W. Shore, and M. D. Perry, "Nanosecond-to-femtosecond laser-induced breakdown in dielectrics," Phys. Rev. B **53**, 1749–1761 (1996).
[39]C. A. Ross, D. G. MacLachlan, D. Choudhury, and R. R. Thomson, "Optimisation of ultrafast laser assisted etching in fused silica," Opt. Express **26**, 24343–24356 (2018).
[40]E. Casamenti, S. Pollonghini, and Y. Bellouard, "Few pulses femtosecond laser exposure for high efficiency 3D glass micromachining," Opt. Express **29**, 35054–35066 (2021).
[41]L. Thiberville, S. Moreno-Swirc, T. Vercauteren, E. Peltier, C. Cavé, and G. Bourg Heckly, "In vivo imaging of the bronchial wall microstructure using fibered confocal fluorescence microscopy," Am. J. Respir. Crit. Care Med. **175**, 22–31 (2007).
[42]C. A. Schneider, W. S. Rasband, and K. W. Eliceiri, "NIH image to ImageJ: 25 years of image analysis," Nat. Methods **9**, 671–675 (2012).
[43]P. Virtanen, R. Gommers, T. E. Oliphant, M. Haberland, T. Reddy, D. Cournapeau, E. Burovski, P. Peterson, W. Weckesser, J. Bright, S. J. van der Walt, M. Brett, J. Wilson, K. J. Millman, N. Mayorov, A. R. J. Nelson, E. Jones, R. Kern, E. Larson, C. J. Carey, İ. Polat, Y. Feng, E. W. Moore, J. VanderPlas, D. Laxalde, J. Perktold, R. Cimrman, I. Henriksen, E. A. Quintero, C. R. Harris, A. M. Archibald, A. H. Ribeiro, F. Pedregosa, P. van Mulbregt, and SciPy 1.0 Contributors, "SciPy 1.0: Fundamental algorithms for scientific computing in Python," Nat. Methods **17**, 261–272 (2020).
[44]I. I. Hirschman and D. V. Widder, *The Convolution Transform* (Courier Corporation, 2012).
[45]See https://www.fujikura.co.uk/ for information about Fujikura CFBs (silica CFB manufacturer); accessed 05 September 2022.
[46]R. R. Thomson, N. D. Psaila, H. T. Bookey, D. T. Reid, and A. K. Kar, "Controlling the cross-section of ultrafast laser inscribed optical waveguides," in *Femtosecond Laser Micromachining: Photonic and Microfluidic Devices in Transparent Materials*, edited by R. Osellame, G. Cerullo, and R. Ramponi (Springer, Berlin, Heidelberg, 2012), pp. 93–125.
[47]See https://i-fiberoptics.com/fiber-detail-asahi.php?id=3305&sum=162 for information about MCL-1500-1.75 CFB (polymer CFB from Asahi Kasei); accessed 01 September 2022.
[48]C. Yavuz, S. N. B. Oliaei, B. Cetin, and O. Yesil-Celiktas, "Sterilization of PMMA microfluidic chips by various techniques and investigation of material characteristics," J. Supercrit. Fluids **107**, 114–121 (2016).
[49]J. D. Hunter, "Matplotlib: A 2D graphics environment," Comput. Sci. Eng. **9**, 90–95 (2007).
[50]C. R. Harris, K. J. Millman, S. J. van der Walt, R. Gommers, P. Virtanen, D. Cournapeau, E. Wieser, J. Taylor, S. Berg, N. J. Smith, R. Kern, M. Picus, S. Hoyer, M. H. van Kerkwijk, M. Brett, A. Haldane, J. F. del Río, M. Wiebe, P. Peterson, P. Gérard-Marchant, K. Sheppard, T. Reddy, W. Weckesser, H. Abbasi, C. Gohlke, and T. E. Oliphant, "Array programming with NumPy," Nature **585**, 357–362 (2020).